

Using Limited Neural Networks to Assess Relative Mechanistic Influence on Shock Heating in Granular Solids

Brenden W. Hamilton* and Timothy C. Germann

*Theoretical Division, Los Alamos National Laboratory, Los Alamos, New Mexico 87545,
USA*

E-mail: brenden@lanl.gov

Abstract

The rapid compaction of granular media results in localized heating that can induce chemical reactions, phase transformations, and melting. However, there are numerous mechanisms in play that can be dependent on a variety of microstructural features. Machine learning techniques such as neural networks offer a ubiquitous method to develop models for physical processes. Limiting what kinds of microstructural information is used as input and assessing normalized changes in network error, the relative importance of different mechanisms can be inferred. Here we utilize binned, initial density information as network inputs to predict local shock heating in a granular high explosive trained from large scale, molecular dynamics simulations. The spatial extent of the density field used in the network is altered to assess the importance and relevant length scales of the physical mechanisms in play, where different microstructural features result in different predictive capability.

The rapid compaction of granular solids can lead to a wide variety of microstructural¹⁻⁴ and chemical⁵⁻⁸ responses that are highly dictated by the initial local packing and structure of the material. While the use of molecular dynamics (MD) and continuum mechanics simulations have helped to elucidate the governing processes,⁹⁻¹⁶ the wide range of mechanisms in play have prevented a unified understanding of events, especially the weighted relevance of various mechanisms.

A key example is the shock compression of energetic materials, in which the materials are typically utilized as neat or polymer bonded granular solids with a bimodal grain size distribution of larger grains and smaller “fills”.¹⁷⁻¹⁹ The shock initiation of chemistry, which can lead to a run to detonation, is governed by the formation of localizations of excess energy known as hotspots, which are typically defined by their temperature and size.^{20,21} These hotspots form through shock induced processes such as intra- and inter-granular void collapse, shear band formation, jetting of material, and inter-granular friction.²²⁻²⁶ From system to system, these individual processes can be influenced by material orientations, crystal defect formation, surface properties, and void shapes and sizes.²⁷⁻³³ Void collapse is typically the dominant process, with the energy localization increasing with increasing P-V work done.³⁴ Hence, broadly understanding the overall shock compression and initiation involves a wide range of materials models and highly detailed structural information.

Additionally, shock compaction not only localizes thermal energy, but can also deform individual molecules, causing them to exist in strained states.³⁵ These intra-molecular strains can alter reaction kinetics and pathways through mechanochemistry.³⁶⁻³⁸ Interestingly, these strain energies are thought to occur through fundamentally different processes than temperature localization.^{33,39} Being able to predict the localization of both temperature and strain energy in a hotspot remains a grand challenge for the energetic materials community and is highly relevant to general materials compaction problems. Being able to predict these processes without running computationally expensive molecular dynamics and hydro-code simulations, as well as to better evaluate the key/necessary mechanisms, is crucial to the materials physics and condensed matter chemistry communities.

Materials science has recently experienced a rapid increase in the use of machine learning (ML) to extract and understand physical processes that can occur.⁴⁰⁻⁴² ML has played a key role in the development of computational models,⁴³⁻⁴⁹ predicting properties,⁵⁰⁻⁵⁴ and characterizing materials.⁵⁵⁻⁵⁸ While predictions from large and non-linear neural networks typically function as a black box, limiting and altering the physical information that informs the network can help to tease out which properties and mechanisms are critical to a processes by the network’s ability to make predictions given its limited subset of input information. This process, employed here, is similar to a “leave one feature out” scheme.

Here, we utilize non-reactive, all-atom MD simulations to model the shock response of the granular high explosive 1,3,5-triamino-2,4,6-trinitrobenzene (TATB). Simulation details are provided in the Methods section and Supplemental Materials section SM-1. A neural network is used to predict the final temperature and intra-molecular strain energy fields given just the initial density field of the unshocked system. The level of coarsening and total extent of the density information given is varied to assess the amount of local information needed to properly predict energy localization from granular compaction. Increasing density resolution provides more information pertaining to pore shape and local curvature, but using only density restricts potentially critical information such as local orientation and crystalline

defects. It should be noted that the purpose of this work is not to minimize the error of the networks and make the best model possible. It is to systematically change the inputs given to the network such that physical trends and important physico-chemical mechanisms can be inferred from the relative change in each network’s predictive ability. However, this methodology does necessitate the network predictions be reasonable accurate as a baseline for extracting materials physics, such that the model is presumable learning some description of the physics.

Predictions of temperature (T) and intra-molecular strain energy (U_{Latent}) fields are done with a simple, non-linear neural network. The system is binned in a Lagrangian fashion on the initial frame prior to shock to provide the density descriptors. From the simulation, each molecule has a defined time it is "shocked", and a "composite frame" is constructed by taking the position and thermodynamics at each molecule at 5ps after its shocked time, i.e. molecules are taken from different simulation frames such that they are at the same relative time compared to being compressed.

The input layer consists of the density of a bin and its N sets of nearest neighbors (initial frame), as shown in Figure 1 for the $N = 1$ case (a second shell of bins would be $N = 2$ and just the central bin, no neighbors, is $N = 0$). Bins with zero molecules are considered as neighbor bins but not as center bins as they will not have a final temperature/energy for an output. The output layer is either the T or U_{Latent} of the center bin (composite frame); each of these two values is trained with separate networks of the same architecture. All networks consist of an input layer of size $(2N + 1)^2$, an output layer of size 1, and a single hidden layer of size $\lfloor 0.5(2N + 1)^2 \rfloor$. Figure 1 exemplifies how the all-atom structure is encoded into the neural network input layer, where the output layer corresponds to a region of the all-atom results, the same center Lagrangian bin, which has mean T and U_{Latent} values. Additional details on network architecture are available in the Methods section and Supplemental Materials section SM-2.

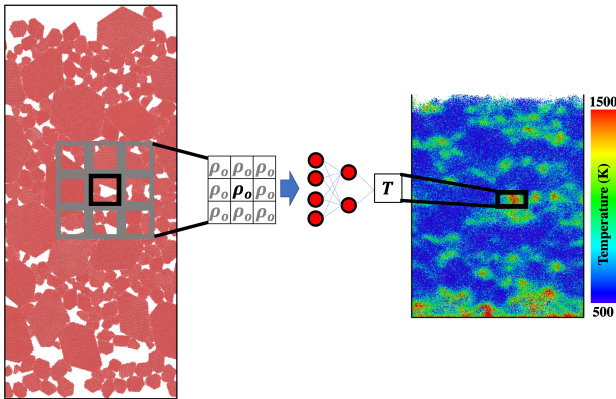


Figure 1: Initial configuration and composite temperature map for the testing set system with example binning for network input and output.

Different square bin sizes of 2.5 nm, 3.0 nm, 4.0 nm and 5.0 nm are used. To compare different bin size results, we define the spatial extent (SE) of the input layer, where $SE = L(N + \frac{1}{2})$ where L is the bin length and N is the number of sets of nearest neighbor bins included. This is the equivalent to the radius of an inscribed circle for the total square of

bins used. Figure 2 shows parity plots of T and U_{Latent} for $L = 5.0$ nm and 2.5 nm with nearly equivalent spatial extents of 27.5 and 26.25 nm, respectively. For the temperature (left column plots), both show decent correlation with the parity line, with RMS errors of 84.4 K and 108.9 K for 5.0 and 2.5 nm bins, respectively, where peak (individual) molecular temperatures in the hotspots are near 2000 K and 600-700 K in the bulk shocked materials.

When comparing the two sets at different bin sizes, it is crucial to consider that while the 2.5 nm bins results in four times as many training and testing points, it also samples a much wider range of values, as the smaller bins provide less smoothing of extreme temperatures. The 2.5 nm cases have considerably more values above 1000 K and its peak hotspot temperatures are much higher than the bulk temperature, relative to the 5.0 nm bins. Both cases mostly have slight over-predictions of values around 800 K and under-predictions for those above 1000 K.

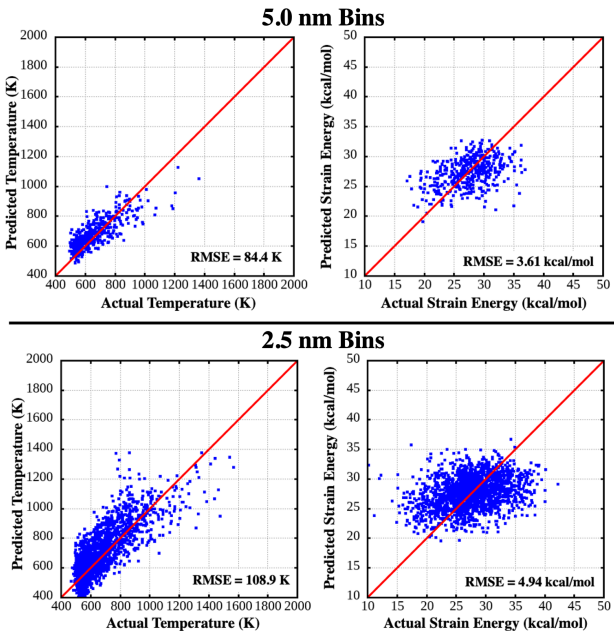


Figure 2: Parity plots of T and U_{Latent} for the 5.0 nm bins and 2.5 nm bins for spatial extents of 27.5 and 26.25 nm, respectively. Data consists of predictions of the smaller MD cell used exclusively for testing.

For the U_{Latent} predictions shown in Figure 2, there is considerably less correlation with the parity line. The predictions even appear to be less correlated overall at the smaller bin sizes. While the U_{Latent} fields, shown in Supplemental Materials section SM-4, are more disperse than the T fields, there are still notable regions of higher and lower strain energy. The predicted fields are considerably more homogeneous and noisy, showing that the density field alone is not enough to predict the mechanisms that drive molecules to bent and distorted shapes, and that more complicated microstructural or thermodynamic information is likely needed to make these predictions. This additionally helps to verify previous results that concluded that the T and U_{Latent} forming mechanisms are different, as their localizations do not occur on a one-to-one basis.³⁵ U_{Latent} also has a strong influence from pore size at larger pores,³³ and the system sizes here may not be large enough to provide a wide enough range

of examples in the training set. Compared to temperature, the density (and therefore P-V work) alone is not enough to make decent quantitative predictions of the U_{Latent} field.

Figure 3 shows heat maps of the actual and predicted temperatures, as well as the difference, for a 2.5 nm bin case. Other bin size and nearest neighbor cases are available in Supplemental Materials section SM-3. From this, it can be assessed that hotspots that are longer in the shock direction, like points (a) and (b) in Figure 3, are under-predicted. However, hotspots that are longer in the cross direction, like points (c) and (d) in Figure 3, are over-predicted. The initial microstructure of this case is shown in Figure 1. Vertical pores and high aspect curvature pores can often result in molecular jetting, leading to high levels of expansion before getting re-compressed,^{23,31,59} however, wider or more circular pores often result in a more hydrodynamic or plastic flow type responses that incurs much less P-V work during re-compression relative to the jetted material, especially as material will have less physical space to expand into the pore before getting re-compressed. It should be noted that, while there is under predictions of the hottest hotspots and over prediction of the colder ones, the model still generally predicts vertical pores to be hotter than the horizontal ones.

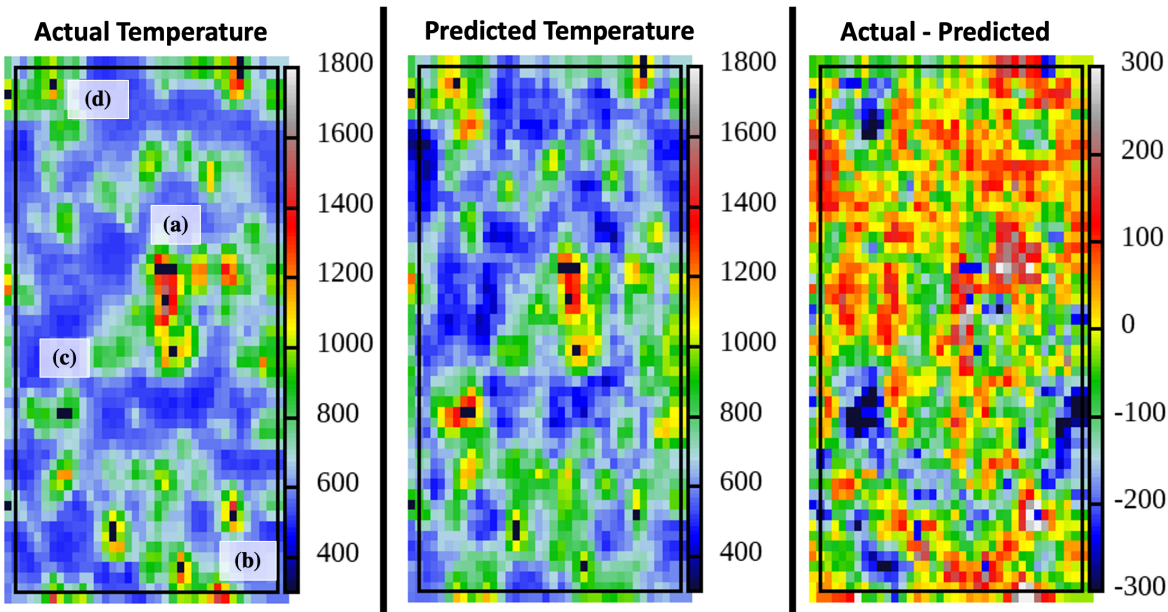


Figure 3: Heat maps of the actual and predicted temperatures, as well as the difference between the two, for the 2.5 nm bin case with a 26.25 nm spatial extent. Points a-d on the actual temperature map correspond to specific hotspots where a and b are under-predicted, and c and d are over-predicted.

The two key factors in qualitatively predicting hotspot temperatures from pore collapse are the pore size and shape.^{9,23,33} Based on these results, the predictions here appear to be fully considering size with the largest pores (points (a) and (c)) predicting high temperatures and the smaller pores typically predicting lower temperatures. Molecular jetting, which greatly influences material expansion into pores, is a much more complex mechanical process where things like curvature of the pore come into play.^{23,31} Even with small initial bins, this

information is partially coarsened out, preventing the network from making these predictions. Information on the shock wave structure/shape, which will change as it progresses over the material, is also unknown to the network and can cause different amounts of shock focusing that leads to jetting. Additionally, the network does not have information related to crystal orientation, which results in changes in hotspot temperature on the order of the errors shown here,²⁸ however, the grain orientations chosen here minimize anisotropy between grains. Hence, while P-V work from pore size is enough to make decently quantitative predictions of hotspot temperature, the finer microstructural details are likely needed to correct for errors on the order of several hundred Kelvin. It is most likely a combination of these omitted features that drives the error in predictions, especially the under-prediction of the highest temperature hotspots.

Figure 4 shows root mean square (RMS) errors and Linear Normalized RMS errors (LN-RMSE) for all networks trained. The LN-RMSE are RMSE values normalized by the RMSE of the linear regression between the density of a bin (no nearest neighbor information) and the temperature. For the top row in Figure 4, which is temperature, we interestingly see, for small to intermediate spatial extent, similar RMSE from all bin sizes, followed by a divergence of values. The slight uptick in errors for large spatial extent are attributed to a static stopping criteria based on error reduction over the previous 200 epochs. For larger SE, the network itself is proportionally larger and potentially learns at a slower rate, especially for smaller bin sizes where N is much larger for a given SE and the network size grows as N^2 .

For an equal spatial extent between two different bin sizes, the smaller bin will result in more training/testing data for a given simulation size. However, the smaller bin system is also less coarse grained, and will have a wider range of peak temperatures and more pronounced temperature gradients. Hence, with more training data and more resolved microstructural data from the density input, the smaller bins are able to reach roughly the same level of predictive power as for the much smoother fields of the larger bins. For the LN-RMSE, as smaller bins will have more variability in temperature with density and therefore a larger normalizing constant, the smallest bin cases perform the best. This normalized case shows the predictive power of adding more microstructural information with a finer density field. As there is significantly less accuracy in the U_{Latent} predictions, the trends of decreasing errors with SE and various bin size effects are less physically meaningful. Plots of RMSE and LN-RMSE for U_{Latent} are available in Supplemental Materials section SM-5. These show similar trends with SE to temperature, yet opposite trends with respect to bin size, which is most likely an effect of coarsening significant noise and the ease of predicting a more uniform field.

In summary, MD simulations of shock compaction of a granular material resulted in heterogeneous localization of both temperature and intra-molecular strain energy, where the latter is known to be responsible for mechanochemical effects. A Lagrangian binning of initial microstructures was used to embed local density information, but intentionally excludes information pertaining to local crystal structure, defects, orientation, and incident wave structure. These density bins were utilized as an input layer to a neural network to predict the shock induced T and U_{Latent} fields.

From trends in RMS errors for different bin sizes and spatial extents of the input layer, we find that the predictability of a network increases with more spatial extent, as well

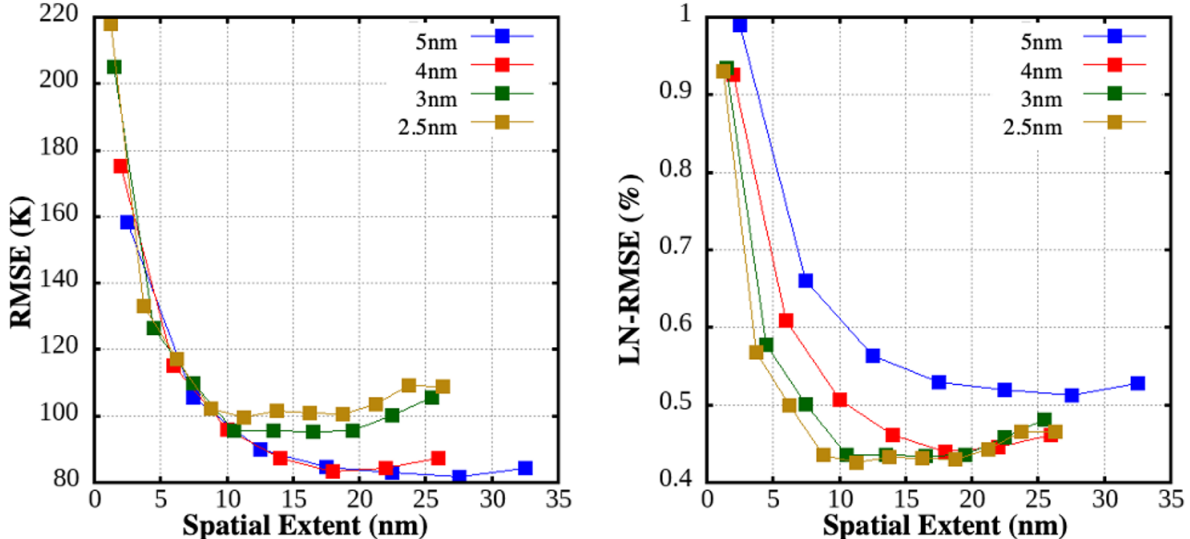


Figure 4: Root mean square errors for all temperature networks run, as a function of spatial extent. Colored lines represent different bin sizes. LN-RMSE (Linear Normalized RMSE) are RMS errors that are normalized by the RMS error of a linear network for zero nearest neighbors ($N = 0$).

as with smaller bins which would carry more precise microstructural information. These improvements are despite the smaller bins leading to much larger variability and fluctuation in the temperature fields, where larger bins smooth and coarsen that information.

While density information did not allow for accurate prediction of U_{Latent} , the networks readily predicted the temperature fields with some of the hotspots being over-predicted, while others are under-predicted. While the network predicts hotter temperatures for larger pores, where more P-V work can occur during compaction, it fails to fully capture other mechanisms such as jetting and molecular ejecta, which can lead to extreme temperatures. This failure manifests in pores that nucleate these jetting mechanisms, those elongated in the shock direction, to have under-predicted temperatures. Additionally, equi-axed or wider pores that do not jet are slightly over-predicted. This leads the network to give less variation in prediction from hotspot to hotspot, but still captures the general trend with pore size.

Hence, we are able to utilize neural network predictions to show that, while P-V work is the dominant mechanism in temperature localization, not having finer microstructural details such as those on the nanometer to sub-nanometer length scale leads to errors with the hotspot on the order of a few hundred Kelvin. Additionally, P-V work and pore shape are shown to be much less important mechanisms for the U_{Latent} field, which may have considerable influence from plasticity levels and material flow rate.^{25,33}

This work shows promise in the use of these limited neural networks to assess physical mechanisms in play for complex, physico-chemical processes in condensed matter systems. In future work, a wider variety of input descriptors can be utilize that, in addition to density, map features such as crystal orientation, pre-existing crystalline defects, surface roughness in pores, and the structure/shape of the incident shock wave which will be altered from upstream microstructural features and shock instabilities. By coupling these features with

a 'leave one feature out' type scheme and the varying spatial extend scheme used here, a relative importance of key hotspot mechanisms and their necessary descriptors can be deduced.

Methods

All simulations were run with all-atom MD using the LAMMPS software package.^{60,61} Interatomic interactions were calculated using the nonreactive, nonpolarizable forcefield from Bedrov et al.,⁶² with tailored harmonic bond stretch and angle bend terms⁶³ and an intramolecular O-H repulsion term.⁶⁴ Electrostatics were solved for in real space with the Wolf potential.⁶⁵ Van der Waals interactions were modeled using the Buckingham potential. All simulations are conducted with a 0.25 fs timestep.

Simulations cells of granular TATB were built with the PBXGen algorithm¹⁷ using columnar grains with a bimodal grain size distribution with peaks at 40 nm and 8 nm. The smaller 'fill' grains make up roughly 2/3 of the total grain count. All grains are crystallographically oriented so that the TATB [001] direction is in the periodic Z direction with thickness 4.1 nm (into the page in the Figures 1 and 3), which minimizes grain-to-grain anisotropy. Two cells were constructed with different sizes of 100 x 400 nm (12440592 atoms), and 100 x 200 nm (6183984 atoms), where the larger system is used to make up the training set and smaller system is the testing set

Shock simulations are conducted using the reverse ballistic method with a particle velocity of 2.0 km/s, with the resulting shock traveling in the $+Y$ direction (upwards in the Figures 1 and 3). The Y direction is a free boundary, whereas the other directions are periodic. Analysis is conducted using a per molecule basis, using the molecular center of mass as its position. Temperature (T) is the molecular roto-vibrational kinetic energy in units of Kelvin. Intra-molecular strain energy (U_{Latent}) is defined as the excess intra-molecular potential energy with respect to the equi-partition theorem.²⁸ Supplemental Materials section SM-1 provides additional MD and PBXGen methods.

For the neural networks, a sigmoid function is used into the hidden layer, and a linear function into the output layer. A bias is allowed for both layers. Supplemental Materials section SM-2 provides additional machine learning method details.

Acknowledgments

Funding for this project was provided by the Director's Postdoctoral Fellowship program at Los Alamos National Laboratory, project LDRD 20220705PRD1. Partial funding was provided by the Advanced Simulation and Computing Physics and Engineering Models project (ASC-PEM). This research used resources provided by the Los Alamos National Laboratory (LANL) Institutional Computing Program. This work was supported by the U.S. Department of Energy (DOE) through LANL, which is operated by Triad National Security, LLC, for the National Nuclear Security Administration of the U.S. Department of Energy (Contract No. 89233218CNA000001). Approved for Unlimited Release LA-UR-23-24466.

Supplemental Material

SM-1: Extended MD Methods

Initial simulation cells, built with the PBXGen algorithm¹, consist purely of TATB grains. The cell is set to be thin in the Z direction, which is periodic. Grains are columnar along the Z axis, and all grains are crystallographically set that the [001] direction is long Z. The X-Y face is randomly oriented for each grain to increase anisotropy.

PBXGen is initialized to insert a bimodal distribution of grains with peak sizes at 40 nm and 8 nm. In both systems generated, the larger grains account for roughly 2/3 of the total mass. The two cells final structure are sizes of 100 x 400 nm (12440592 atoms) and 100 x 200 nm (6183984 atoms).

As PBXGen packed particles typically only have a volumetric packing density of around 50%, the initial cell sizes were 200x400 nm and 200x200 nm. The X direction was then compacted to the final size over a period of 250 ps. Temperature was set 500 K to promote grain boundary formation and help anneal defects formed during compaction. Atom coordinates were fractionally remapped at every step during compaction. The final cells were thermalized at 300 K for 25 ps.

Shock simulations were conducted along the Y axis (long direction) using a momentum mirror on the bottom box boundary and a free boundary at the top. The X and Z directions remained periodic.

All trajectory analysis for building training and testing sets were done on a molecular basis. The molecule center of mass was used for position, and the center of mass velocity for velocity. We define C.O.M. properties with capital letters and atomic properties with lowercase letters. From the per atom velocities, we compute three kinetic energy values: the total, translational, and roto-vibrational:

$$KE_{Tot} = \sum \frac{1}{2} m_i (v_i \cdot v_i)$$
$$KE_{Trans} = \frac{1}{2} M (V_i \cdot V_i)$$
$$KE_{ro-vib} = KE_{Tot} - KE_{Trans}$$

Where m and M are atomic and molecular mass, and v and V are velocity vectors. Subscript i designates each atom, which the sum is over. Temperature is defined as the roto-vibrational kinetic energy in units of kelvin from the classical specific heat:

$$KE_{ro-vib} = \frac{3N - 3}{2} k_B T$$

The composite trajectory frame is taken as molecular properties at the time for each molecule of $t_0 + 5$ ps where t_0 is the time in which the molecule is shocked. We define shocked time as the first frame in which a molecule has a C.O.M. velocity between -0.3 and 0.3 km/s for three consecutive frames (0.3 ps). This ensures that the molecule is at rest, which is shocked in the reverse ballistic frame used here. Additionally, molecules that are pushed into a void are treated as shocked only after material has recompressed on the downstream face of a pore. This leads to

+ 5 ps to be a measure of 5 ps after shock heating. This minimizes the effects from local thermal transport and pressure relaxation events.

SM-2: Extended ML Methods

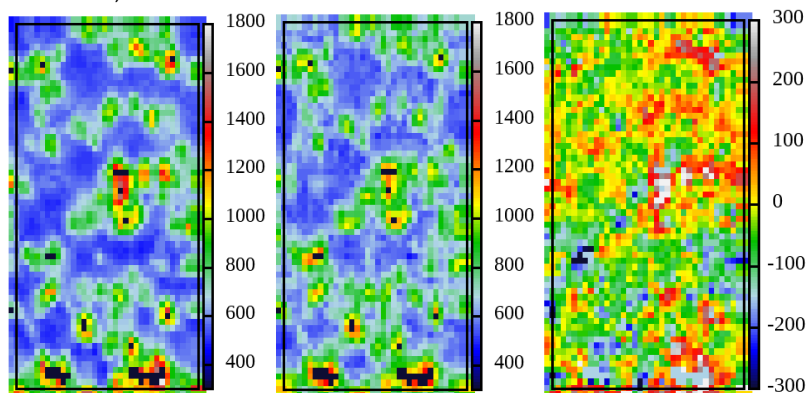
Neural networks are defined to have a variable sized input and hidden layer. The input layer is of size $N+1$, where N is the number of neighbor bins used. The hidden layer is over size $\lfloor 0.5(N + 1) \rfloor$. For the no nearest neighbor case ($N+1=1$), the input and hidden layer are set to have size of 1. A sigmoid function is used from input to the hidden layer. The output layer is always size one, and a linear function connects the hidden and output layer. A biasing value is allowed for both functions.

The larger of the two MD systems is used as the training set. An 80-20 split is used during training. An early stopping criterion is set to stop training and take the best network if the mean square error of the 20% testing group does not drop by at least 0.00001 over 100 epochs. This error delta is in normalized units, where all input/output data is utilized as the Z-score of the data. An Adam optimizerⁱⁱ is used with a 1×10^{-3} learning rate. All errors values presented in this work are based on predictions of the smaller of the MD systems which is not included in training at all.

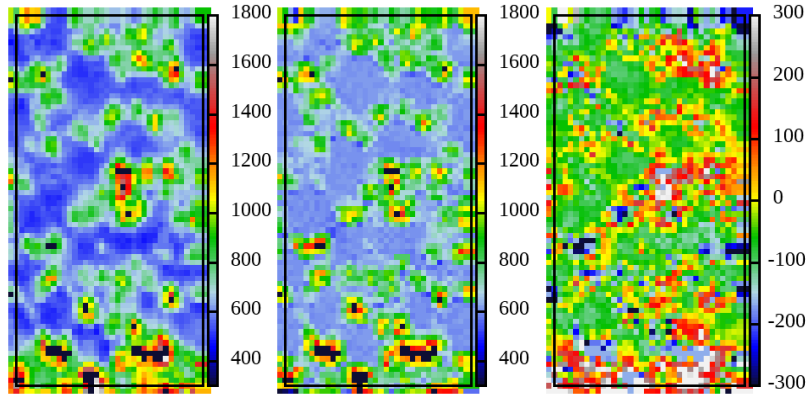
Within the input layer for a given network, the order of the bins is constant in the input layer, such that the network can differentiate upstream and downstream of the bin, as well as some information regarding shape of a pore.

SM-3: Temperature Prediction Heat Maps

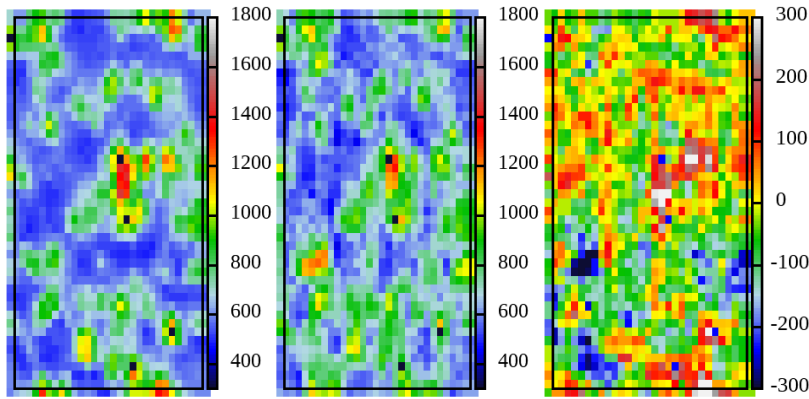
Bin = 2.5 nm, 5 NN



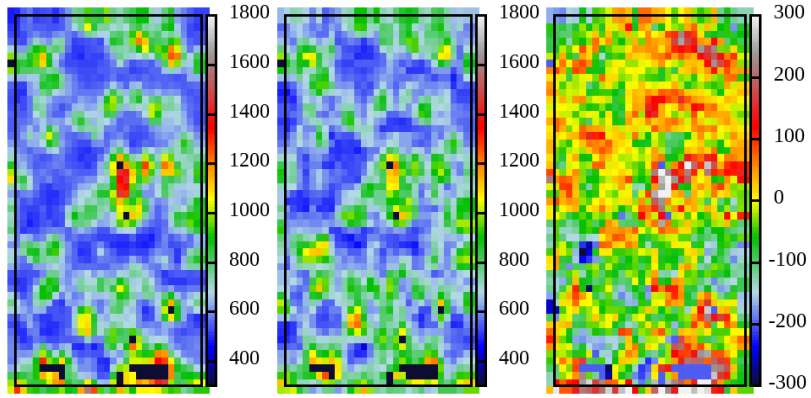
Bin = 2.5nm, 1 NN



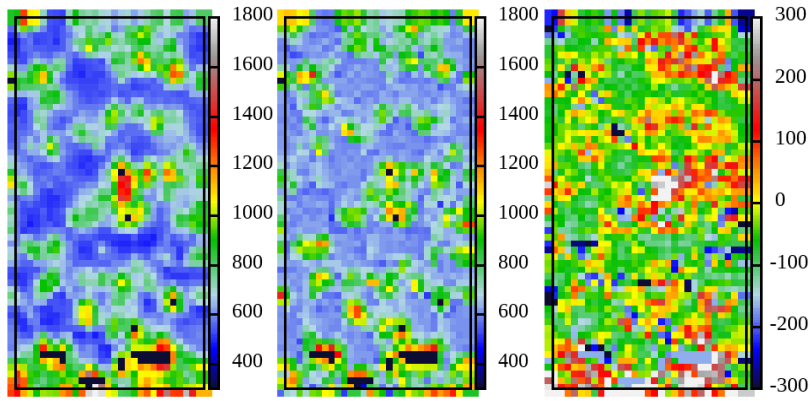
Bin = 3.0nm, 8 NN



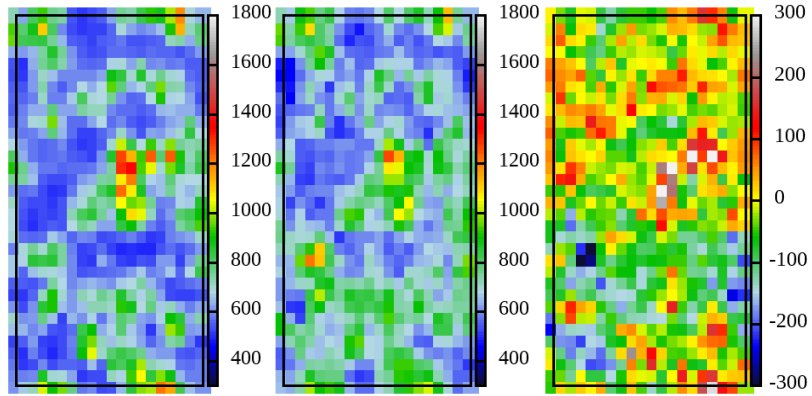
Bin=3.0nm, 4 NN



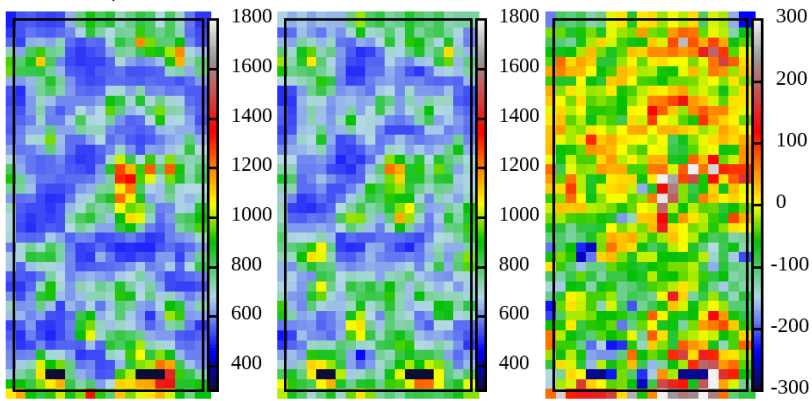
Bin = 3.0nm, 1 NN



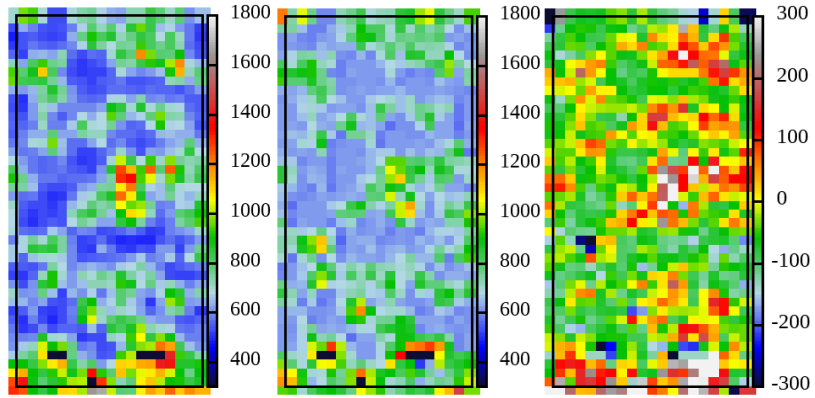
Bin = 4.0nm, 6 NN



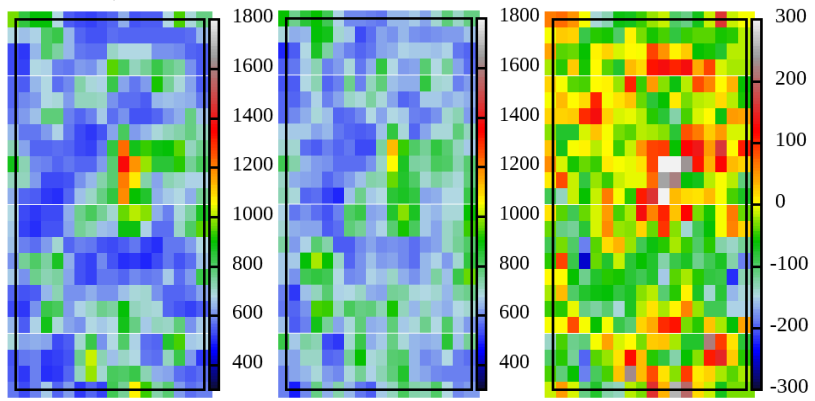
Bin = 4.0nm, 3 NN



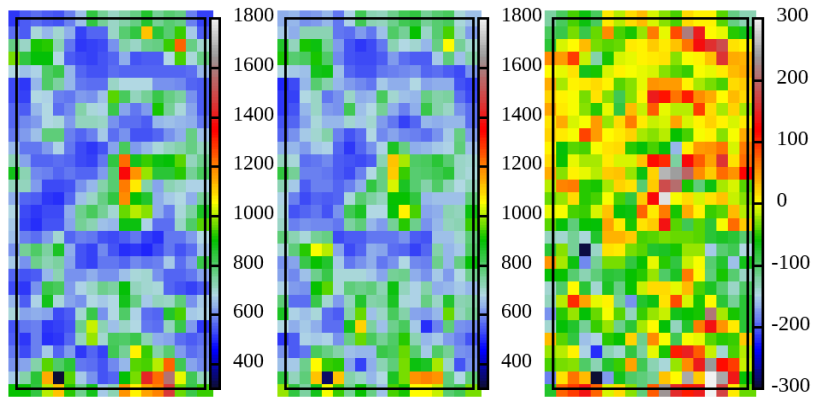
Bin = 4.0nm, 1 NN



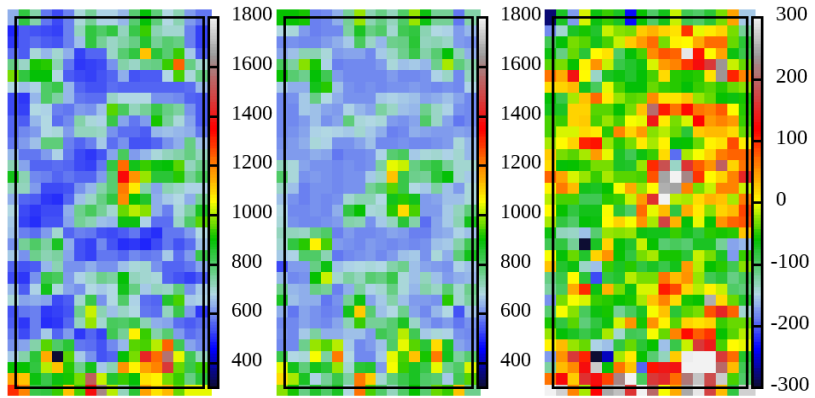
Bin = 5.0nm, 6 NN



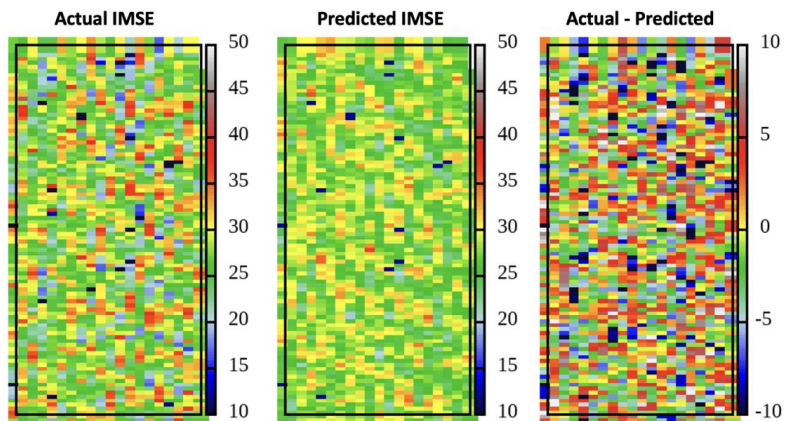
Bin = 5.0nm, 3 NN



Bin = 5.0nm, 1 NN

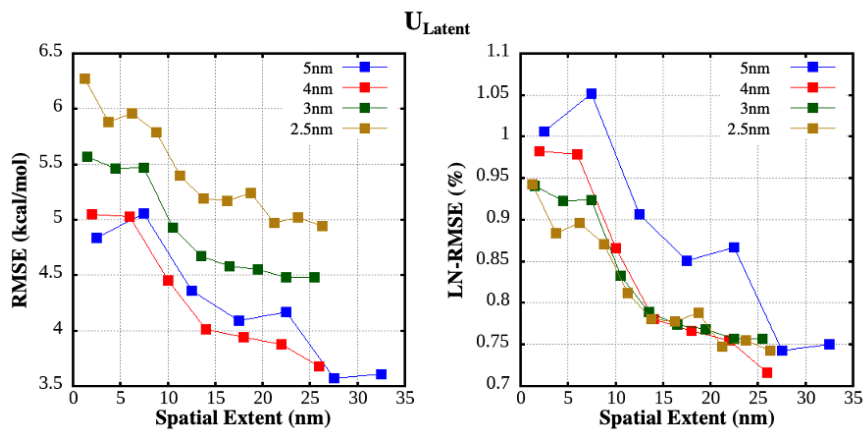


SM-4: U_{Latent} Prediction Heat Maps



SM Figure XXX:

SM-5: U_{Latent} RMSE Values



References

References

- (1) Cherukara, M. J.; Germann, T. C.; Kober, E. M.; Strachan, A. Shock Loading of Granular Ni/Al Composites. Part 1: Mechanics of Loading. *Journal of Physical Chemistry C* **2014**, *118*, 26377–26386.
- (2) Brujić, J.; Wang, P.; Song, C.; Johnson, D. L.; Sindt, O.; Makse, H. A. Granular dynamics in compaction and stress relaxation. *Physical review letters* **2005**, *95*, 128001.
- (3) Lumay, G.; Vandewalle, N. Experimental study of granular compaction dynamics at different scales: grain mobility, hexagonal domains, and packing fraction. *Physical review letters* **2005**, *95*, 028002.
- (4) Busignies, V.; Tchoreloff, P.; Leclerc, B.; Hersen, C.; Keller, G.; Couarraze, G. Compaction of crystallographic forms of pharmaceutical granular lactoses. II. Compacts mechanical properties. *European journal of pharmaceutics and biopharmaceutics* **2004**, *58*, 577–586.
- (5) Cherukara, M. J.; Germann, T. C.; Kober, E. M.; Strachan, A. Shock Loading of Granular Ni/Al Composites. Part 2: Shock-Induced Chemistry. *Journal of Physical Chemistry C* **2016**, *120*, 6804–6813.
- (6) Strachan, A.; van Duin, A. C.; Chakraborty, D.; Dasgupta, S.; Goddard, W. A. Shock Waves in High-Energy Materials: The Initial Chemical Events in Nitramine RDX. *Physical Review Letters* **2003**, *91*, 7–10.
- (7) Yang, Y.; Gould, R.; Horie, Y.; Iyer, K. Shock-induced chemical reactions in a Ni/Al powder mixture. *Applied physics letters* **1997**, *70*, 3365–3367.
- (8) Zhou, X.; Miao, Y. R.; Shaw, W. L.; Suslick, K. S.; Dlott, D. D. Shock Wave Energy Absorption in Metal-Organic Framework. *Journal of the American Chemical Society* **2019**, *141*, 2220–2223.
- (9) Wood, M. A.; Kittell, D. E.; Yarrington, C. D.; Thompson, A. P. Multiscale modeling of shock wave localization in porous energetic material. *Physical Review B* **2018**, *97*, 014109.
- (10) Herring, S. D.; Germann, T. C.; Grønbech-Jensen, N. Effects of void size, density, and arrangement on deflagration and detonation sensitivity of a reactive empirical bond order high explosive. *Physical Review B* **2010**, *82*, 214108.
- (11) Rai, N. K.; Sen, O.; Udaykumar, H. S. Macro-scale sensitivity through meso-scale hotspot dynamics in porous energetic materials: Comparing the shock response of 1,3,5-triamino-2,4,6-trinitrobenzene (TATB) and 1,3,5,7-tetranitro-1,3,5,7-tetrazoctane (HMX). *Journal of Applied Physics* **2020**, *128*, 1–24.
- (12) Bidault, X.; Pineau, N. Granularity impact on hotspot formation and local chemistry in shocked nanostructured RDX. *Journal of Chemical Physics* **2018**, *149*.

- (13) Xiong, Y.; Li, X.; Xiao, S.; Deng, H.; Huang, B.; Zhu, W.; Hu, W. Molecular dynamics simulations of shock loading of nearly fully dense granular Ni-Al composites. *Physical Chemistry Chemical Physics* **2019**, *21*, 20252–20261.
- (14) Pouliquen, O.; Belzons, M.; Nicolas, M. Fluctuating particle motion during shear induced granular compaction. *Physical review letters* **2003**, *91*, 014301.
- (15) Kadau, K.; Germann, T. C.; Lomdahl, P. S.; Albers, R. C.; Wark, J. S.; Higginbotham, A.; Holian, B. L. Shock waves in polycrystalline iron. *Physical Review Letters* **2007**, *98*, 135701.
- (16) Rutherford, M. E.; Chapman, D. J.; Derrick, J. G.; Patten, J. R.; Bland, P. A.; Rack, A.; Collins, G. S.; Eakins, D. E. Probing the early stages of shock-induced chondritic meteorite formation at the mesoscale. *Scientific reports* **2017**, *7*, 1–10.
- (17) Li, C.; Hamilton, B. W.; Shen, T.; Alzate, L.; Strachan, A. Systematic Builder for All-Atom Simulations of Plastically Bonded Explosives. *Propellants, Explosives, Pyrotechnics* **2022**, *47*, e202200003.
- (18) Skidmore, C.; Phililips, D.; Howe, P.; Mang, J.; Romero, J. The Evolution of Microstructural Changes in Pressed HMX Explosives. Eleventh International Detonation Symposium. Snowmass, Colorado, 1998.
- (19) Willey, T. M.; Van Buuren, T.; Lee, J. R.; Overturf, G. E.; Kinney, J. H.; Handly, J.; Weeks, B. L.; Ilavsky, J. Changes in pore size distribution upon thermal cycling of TATB-based explosives measured by ultra-small angle X-ray scattering. *Propellants, Explosives, Pyrotechnics* **2006**, *31*, 466–471.
- (20) Hamilton, B. W.; Sakano, M. N.; Li, C.; Strachan, A. Chemistry Under Shock Conditions. *Annual Review of Materials Research* **2021**, *51*, 101–130.
- (21) Handley, C. A.; Lambourn, B. D.; Whitworth, N. J.; James, H. R.; Belfield, W. J. Understanding the shock and detonation response of high explosives at the continuum and meso scales. *Applied Physics Reviews* **2018**, *5*, 011303.
- (22) Davis, W. C. High Explosives The Interaction of Chemistry and Mechanics. *Los Alamos Science* **1981**, *2*, 48–75.
- (23) Li, C.; Hamilton, B. W.; Strachan, A. Hotspot formation due to shock-induced pore collapse in 1,3,5,7-tetranitro-1,3,5,7-tetrazoctane (HMX): Role of pore shape and shock strength in collapse mechanism and temperature. *Journal of Applied Physics* **2020**, *127*, 175902.
- (24) Cawkwell, M. J.; Sewell, T. D.; Zheng, L.; Thompson, D. L. Shock-induced shear bands in an energetic molecular crystal: Application of shock-front absorbing boundary conditions to molecular dynamics simulations. *Physical Review B* **2008**, *78*, 014107.
- (25) Kroonblawd, M. P.; Fried, L. E. High Explosive Ignition through Chemically Activated Nanoscale Shear Bands. *Physical Review Letters* **2020**, *124*, 206002.

- (26) Dienes, J. K. Discussion of a statistical theory of fragmentation processes. *Mechanics of Materials* **1985**, *4*, 337–341.
- (27) Zhao, P.; Lee, S.; Sewell, T.; Udaykumar, H. S. Tandem Molecular Dynamics and Continuum Studies of Shock-Induced Pore Collapse in TATB. *Propellants, Explosives, Pyrotechnics* **2020**, *45*, 196–222.
- (28) Hamilton, B. W.; Kroonblawd, M. P.; Strachan, A. The Potential Energy Hotspot: Effects from Impact Velocity, Defect Geometry, and Crystallographic Orientation. *Journal of Physical Chemistry C* **2022**, *126*, 3743–3755.
- (29) Lafourcade, P.; Denoual, C.; Maillet, J. B. Irreversible Deformation Mechanisms for 1,3,5-Triamino-2,4,6-Trinitrobenzene Single Crystal through Molecular Dynamics Simulations. *Journal of Physical Chemistry C* **2018**, *122*, 14954–14964.
- (30) Grilli, N.; Koslowski, M. The effect of crystal orientation on shock loading of single crystal energetic materials. *Computational Materials Science* **2018**, *155*, 235–245.
- (31) Li, C.; Strachan, A. Shock-induced collapse of porosity, mapping pore size and geometry, collapse mechanism, and hotspot temperature. *Journal of Applied Physics* **2022**, *132*, 065901.
- (32) Bidault, X.; Pineau, N. Impact of surface energy on the shock properties of granular explosives. *Journal of Chemical Physics* **2018**, *148*.
- (33) Hamilton, B. W.; Germann, T. C. Energy localization efficiency in 1, 3, 5-trinitro-2, 4, 6-triaminobenzene pore collapse mechanisms. *Journal of Applied Physics* **2023**, *133*, 035901.
- (34) Holian, B. L.; Germann, T. C.; Maillet, J. B.; White, C. T. Atomistic Mechanism for Hot Spot Initiation. *Physical Review Letters* **2002**, *89*, 285501.
- (35) Hamilton, B. W.; Kroonblawd, M. P.; Li, C.; Strachan, A. A Hotspot’s Better Half: Non-Equilibrium Intra-Molecular Strain in Shock Physics. *Journal of Physical Chemistry Letters* **2021**, *12*, 2756–2762.
- (36) Hamilton, B. W.; Kroonblawd, M. P.; Strachan, A. Extemporaneous Mechanochemistry: Shockwave Induced Ultrafast Chemical Reactions Due to Intramolecular Strain Energy. *Journal of Physical Chemistry Letters* **2022**, *13*, 6657–6663.
- (37) Hamilton, B. W.; Strachan, A. Many-Body Mechanochemistry : Intra-molecular Strain in Condensed Matter Chemistry. *chemRxiv* **2022**,
- (38) Hamilton, B. W.; Germann, T. C. Interplay of Mechanochemistry and Material Processes in the Graphite to Diamond Phase Transformation. *arXiv preprint arXiv:2302.04684* **2023**,
- (39) Hamilton, B. W.; Kroonblawd, M. P.; Macatangay, J.; Springer, H. K.; Strachan, A. Intergranular Hotspots: A Molecular Dynamics Study on the Influence of Compressive and Shear Work. *arXiv preprint arXiv:2302.10728* **2023**,

- (40) Iten, R.; Metger, T.; Wilming, H.; Del Rio, L.; Renner, R. Discovering Physical Concepts with Neural Networks. *Physical Review Letters* **2020**, *124*, 10508.
- (41) Butler, K. T.; Davies, D. W.; Cartwright, H.; Isayev, O.; Walsh, A. Machine learning for molecular and materials science. *Nature* **2018**, *559*, 547–555.
- (42) Zhong, X.; Gallagher, B.; Liu, S.; Kailkhura, B.; Hiszpanski, A.; Han, T. Explainable machine learning in materials science. *npj Computational Materials* **2022**, *8*, 204.
- (43) Huan, T. D.; Batra, R.; Chapman, J.; Krishnan, S.; Chen, L.; Ramprasad, R. A universal strategy for the creation of machine learning-based atomistic force fields. *NPJ Computational Materials* **2017**, *3*, 37.
- (44) Chan, H.; Cherukara, M. J.; Narayanan, B.; Loeffler, T. D.; Benmore, C.; Gray, S. K.; Sankaranarayanan, S. K. Machine learning coarse grained models for water. *Nature Communications* **2019**, *10*, 379.
- (45) Zuo, Y.; Chen, C.; Li, X.; Deng, Z.; Chen, Y.; Behler, J.; Csányi, G.; Shapeev, A. V.; Thompson, A. P.; Wood, M. A., et al. Performance and cost assessment of machine learning interatomic potentials. *The Journal of Physical Chemistry A* **2020**, *124*, 731–745.
- (46) Yoo, P.; Sakano, M.; Desai, S.; Islam, M. M.; Liao, P.; Strachan, A. Neural network reactive force field for C, H, N, and O systems. *npj Computational Materials* **2021**, *7*, 1–10.
- (47) Lindsey, R. K.; Fried, L. E.; Goldman, N. ChIMES: A Force Matched Potential with Explicit Three-Body Interactions for Molten Carbon. *Journal of Chemical Theory and Computation* **2017**, *13*, 6222–6229.
- (48) Hamilton, B. W.; Yoo, P.; Sakano, M. N.; Islam, M. M.; Strachan, A. High Pressure and Temperature Neural Network Reactive Force Field for Energetic Materials. *arXiv preprint arXiv:2302.04906* **2023**,
- (49) Zhang, Y.; Hu, C.; Jiang, B. Embedded atom neural network potentials: Efficient and accurate machine learning with a physically inspired representation. *The Journal of Physical Chemistry Letters* **2019**, *10*, 4962–4967.
- (50) Fernandez, M.; Boyd, P. G.; Daff, T. D.; Aghaji, M. Z.; Woo, T. K. Rapid and accurate machine learning recognition of high performing metal organic frameworks for CO₂ capture. *The Journal of Physical Chemistry Letters* **2014**, *5*, 3056–3060.
- (51) Xie, T.; Grossman, J. C. Crystal graph convolutional neural networks for an accurate and interpretable prediction of material properties. *Physical review letters* **2018**, *120*, 145301.
- (52) Sakano, M. N.; Hamed, A.; Kober, E. M.; Grilli, N.; Hamilton, B. W.; Islam, M. M.; Koslowski, M.; Strachan, A. Unsupervised Learning-Based Multiscale Model of Thermochemistry in 1,3,5-Trinitro-1,3,5-triazinane (RDX). *Journal of Physical Chemistry A* **2020**, *124*, 9141–9155.

- (53) Ward, L.; Agrawal, A.; Choudhary, A.; Wolverton, C. A general-purpose machine learning framework for predicting properties of inorganic materials. *npj Computational Materials* **2016**, *2*, 1–7.
- (54) Zhuo, Y.; Mansouri Tehrani, A.; Brgoch, J. Predicting the band gaps of inorganic solids by machine learning. *The Journal of Physical Chemistry Letters* **2018**, *9*, 1668–1673.
- (55) Carbone, M. R.; Topsakal, M.; Lu, D.; Yoo, S. Machine-learning X-ray absorption spectra to quantitative accuracy. *Physical Review Letters* **2020**, *124*, 156401.
- (56) Timoshenko, J.; Lu, D.; Lin, Y.; Frenkel, A. I. Supervised machine-learning-based determination of three-dimensional structure of metallic nanoparticles. *The Journal of Physical Chemistry Letters* **2017**, *8*, 5091–5098.
- (57) Yao, Y.; Chan, H.; Sankaranarayanan, S.; Balaprakash, P.; Harder, R. J.; Cherukara, M. J. AutoPhaseNN: unsupervised physics-aware deep learning of 3D nanoscale Bragg coherent diffraction imaging. *npj Computational Materials* **2022**, *8*, 1–8.
- (58) Hu, W.; Ye, S.; Zhang, Y.; Li, T.; Zhang, G.; Luo, Y.; Mukamel, S.; Jiang, J. Machine learning protocol for surface-enhanced raman spectroscopy. *The journal of physical chemistry letters* **2019**, *10*, 6026–6031.
- (59) Germann, T. C.; Holian, B. L.; Lomdahl, P. S.; Heim, A. J.; Grønbech-Jensen, N.; Maillet, J.-B. Molecular dynamics simulations of detonation in defective explosive crystals. Proceedings of the Twelfth International Detonation Symposium. 2002; pp 711–717.
- (60) Plimpton, S. Fast parallel algorithms for short-range molecular dynamics. *Journal of Computational Physics* **1995**, *117*, 1–19.
- (61) Thompson, A. P.; Aktulga, H. M.; Berger, R.; Bolintineanu, D. S.; Brown, W. M.; Crozier, P. S.; in 't Veld, P. J.; Kohlmeyer, A.; Moore, S. G.; Nguyen, T. D.; Shan, R.; Stevens, M. J.; Tranchida, J.; Trott, C.; Plimpton, S. J. LAMMPS - a flexible simulation tool for particle-based materials modeling at the atomic, meso, and continuum scales. *Computer Physics Communications* **2022**, *271*, 108171.
- (62) Bedrov, D.; Borodin, O.; Smith, G. D.; Sewell, T. D.; Dattelbaum, D. M.; Stevens, L. L. A molecular dynamics simulation study of crystalline 1,3,5-triamino-2,4,6- trinitrobenzene as a function of pressure and temperature. *Journal of Chemical Physics* **2009**, *131*.
- (63) Kroonblawd, M. P.; Sewell, T. D. Theoretical determination of anisotropic thermal conductivity for crystalline 1,3,5-triamino-2,4,6-trinitrobenzene (TATB). *Journal of Chemical Physics* **2013**, *139*.
- (64) Mathew, N.; Sewell, T. D.; Thompson, D. L. Anisotropy in surface-initiated melting of the triclinic molecular crystal 1,3,5-triamino-2,4,6-trinitrobenzene: A molecular dynamics study. *Journal of Chemical Physics* **2015**, *143*.

- (65) Wolf, D.; Keblinski, P.; Phillpot, S. R.; Eggebrecht, J. Exact method for the simulation of Coulombic systems by spherically truncated, pairwise r-1 summation. *Journal of Chemical Physics* **1999**, *110*, 8254–8282.

Graphical TOC Entry

